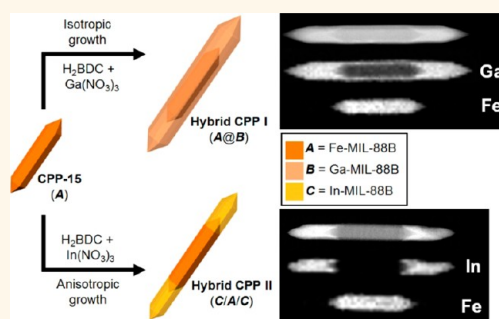


Controlled Isotropic or Anisotropic Nanoscale Growth of Coordination Polymers: Formation of Hybrid Coordination Polymer Particles

Hee Jung Lee,[†] Yea Jin Cho,[†] Won Cho, and Moonhyun Oh*

Department of Chemistry, Yonsei University, 134 Shinchon-dong, Seodaemun-gu, Seoul, 120-749, Korea. [†]These authors contributed equally to this work.

ABSTRACT The ability to fabricate multicompositional hybrid materials in a precise and controlled manner is one of the primary goals of modern materials science research. In addition, an understanding of the phenomena associated with the systematic growth of one material on another can facilitate the evolution of multifunctional hybrid materials. Here, we demonstrate precise manipulation of the isotropic and/or anisotropic nanoscale growth of various coordination polymers (CPs) to obtain heterocompositional hybrid coordination polymer particles. Chemical composition analyses conducted at every growth step reveal the formation of accurately assembled hybrid nanoscale CPs, and microscopy images are used to examine the morphology of the particles and visualize the hybrid structures. The dissimilar growth behavior, that is, growth in an isotropic or anisotropic fashion, is found to be dependent on the size of the metal ions involved within the CPs.



KEYWORDS: nanoscale growth · MOF · core–shell · hybrid material · anisotropic

Porous coordination polymers (CPs) or metal–organic frameworks (MOFs) have been the subject of intense research due to their many fascinating properties and applications, such as gas storage, gas separation, catalysts, and recognition.^{1–7} Currently, various ongoing research has been devoted to the fabrication of nano- and microscaled coordination polymer particles (CPPs)^{8–16} and CP thin films^{17–21} as part of a logical attempt to extend the applicability and to enhance the properties of CPs. Indeed, the smart utilization of nanoscale CPPs as magnetic resonance imaging (MRI) contrast agents and drug delivery vessels in biological systems has recently been demonstrated.^{12–14}

On the other hand, the fabrication of hybrid CP crystals is an important theme in the development of new functional materials because manipulation of the composition and structure of CPs is vital for fine-tuning their properties.^{22–25} As numerous hybrid nanomaterials with more than two components have been suggested as candidates for multifunctional materials with

customized or advanced properties,^{26–29} CPPs with precise heterocompositions will provide a great opportunity to extend the applicability of CPPs and CPs. However, no attempts have been made to study the precise nanoscale growth of CPs for the preparation of hybrid nanoscale CPPs.

In this work, we report on the precise and controlled preparation of heterostructured CPPs through the selective isotropic and anisotropic nanoscale growth of CPs. The research described herein will allow for a greater understanding of multicompositional nanoscale CPPs that could facilitate their eventual use in practical applications.

RESULTS AND DISCUSSION

An examination of the heterometalation of CPPs based on the nanoscale growth of CPs was performed using Fe-MIL-88B³⁰ and two of its analogues, Ga-MIL-88B and In-MIL-88B (Scheme 1). Fe-MIL-88B nanorods (CPP-15, Figure 1a,b), which have a hexagonal 3D structure consisting of trimers of FeO₆ octahedra connected to BDC building blocks, were first prepared *via* a previously

* Address correspondence to moh@yonsei.ac.kr.

Received for review October 4, 2012 and accepted December 6, 2012.

Published online December 14, 2012
10.1021/nn304597h

© 2012 American Chemical Society

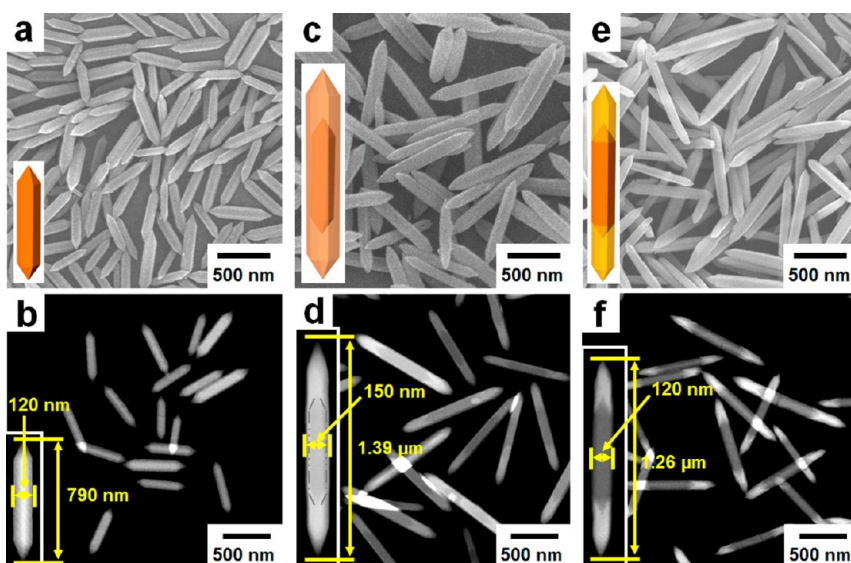
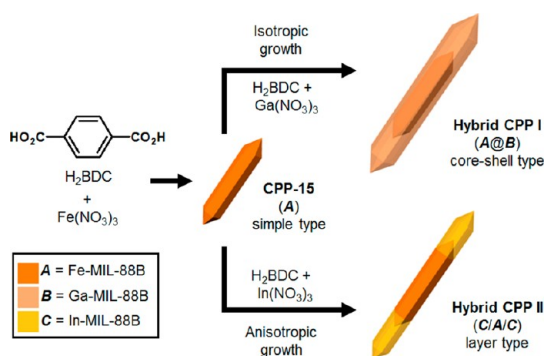


Figure 1. SEM and STEM images of (a,b) initial CPP-15 nanorods, (c,d) core–shell-type heterocompositional Hybrid CPP I (A@B), and (e,f) layer-type heterocompositional Hybrid CPP II (C/A/C). Here, A = Fe-MIL-88B, B = Ga-MIL-88B, and C = In-MIL-88B.

reported solvothermal method using H_2BDC and $\text{Fe}(\text{NO}_3)_3$ precursors.³¹ The resulting **CPP-15** was then used as a seed for the growth of secondary CPs. Consecutive solvothermal reactions of the secondary CP precursors (H_2BDC and $\text{M}(\text{NO}_3)_3$, $\text{M} = \text{Ga}^{3+}$ or In^{3+}) in the presence of the initially prepared Fe-MIL-88B nanorods resulted in the formation of heterocompositional CPPs through hybridization between the initial Fe-MIL-88B and the subsequently formed M-MIL-88B ($\text{M} = \text{Ga}$ or In) (Scheme 1). Field-emission scanning electron microscopy (FE-SEM) and scanning transmission electron microscopy (STEM) images (Figure 1c,d) revealed the formation of CPPs with a rod-shaped morphology similar to that of the initial Fe-MIL-88B seed. In addition, an increase in the size of the particles after the growth of the secondary CPs was clearly observed in the microscopy images. The increase in the length and width (ca. 600 and 30 nm, respectively) of the nanorod after the formation of **Hybrid CPP I**, which was caused by the growth of Ga-MIL-88B on Fe-MIL-88B seed, can be calculated by comparing the length and width of the **Hybrid CPP I** nanorod (Figure 1d) to the initial **CPP-15** nanorod (Figure 1b). This increase in the length and width indicated the formation of core–shell-type hybrid CPPs, Fe-MIL-88B@Ga-MIL-88B, which can be formed as a result of the isotropic growth of secondary CP on the entire surface of the initial **CPP-15**. The contrast light and shade STEM images of **Hybrid CPP I** (Figure 1d) visually showed the formation of core–shell hybrid CPPs. In contrast, an increase in length but not width was observed in the FE-SEM and STEM images of **Hybrid CPP II**, which was obtained by the growth of In-MIL-88B on Fe-MIL-88B seed (Figure 1e,f). The clear contrast light and shade STEM images of **Hybrid CPP II**

(Figure 1f) noticeably revealed the formation of layer-type hybrid nanorods. This layer-type hybrid CPP can be produced as a result of anisotropic growth of In-MIL-88B on the initial **CPP-15**, that is, the growth of In-MIL-88B only in the *c*-direction at both tips of the **CPP-15** nanorods. When the reaction time is increased, no significant size increase of the particles is detected. The size change is comparable to that which occurs during the regular reaction time, because there is no significant amount of precursors remaining after a regular reaction time (20 min). However, the relatively long **Hybrid CPP II** was detected, when the large amount of the secondary CP precursors (H_2BDC and $\text{In}(\text{NO}_3)_3$) was used during the growth of In-MIL-88B (Supporting Information Figure S1).

The chemical composition analyses of **Hybrid CPP I** and **II** supported the formation of heterocompositional A@B core–shell and C/A/C layer-type hybrid CPP crystals (A = Fe-MIL-88B, B = Ga-MIL-88B, C = In-MIL-88B), respectively. Energy dispersive X-ray (EDX) spectra (Supporting Information Figure S2a–c) were acquired at different spots on **Hybrid CPP I**. First, the EDX spectrum obtained for one whole particle (Supporting Information Figure S2a) indicated the production of a new material consisting of gallium atoms in addition to the initial Fe-MIL-88B, as evidenced from the observation of gallium atoms in addition to carbon, oxygen, and iron atoms. Second, the detection of only carbon, oxygen, and gallium atoms, but not iron atoms, in the EDX spectrum measured at the tip of **Hybrid CPP I** (Supporting Information Figure S2b) indicated that the gallium-based material (Ga-MIL-88B) is the only material present in this area. Third, the EDX spectrum for the middle region of **Hybrid CPP I** suggests the presence of both Fe-MIL-88B and Ga-MIL-88B, as evidenced



Scheme 1. Schematic representation of the preparation of two types of heterocompositional CPPs, Hybrid CPP I (A@B) and Hybrid CPP II (C/A/C), through the isotropic and anisotropic nanoscale growth of secondary CPPs on CPP-15. Here, A = Fe-MIL-88B, B = Ga-MIL-88B, and C = In-MIL-88B

by the detection of both iron and gallium atoms (Supporting Information Figure S2c). The obtained EDX data corroborate the expected chemical compositions for the suggested core–shell structure of **Hybrid CPP I** (Fe-MIL-88B@Ga-MIL-88B). The C/A/C layer-type structure of **Hybrid CPP II** was also confirmed from a series of EDX spectra (Supporting Information Figure S2d–f). The trends observed in the compositions detected for a whole particle and the tip of the **Hybrid CPP II** (Supporting Information Figure S2d,e) were similar to those obtained from **Hybrid CPP I**, indicating the creation of a new material containing indium atoms (In-MIL-88B) at the tip of the particles. However, there was a significant difference between the spectra measured at the center of **Hybrid CPP I** and **II** (Supporting Information Figure S2c,f). Compositions corresponding to only Fe-MIL-88B and not to the new indium-based material were detected at the center of **Hybrid CPP II**, which correlates well with the expected C/A/C layer-type hybrid crystal. If **Hybrid CPP II** is a core–shell structure, indium atoms must be detected at the center of the sample, as shown for **Hybrid CPP I**.

Additional evidence for the production of core–shell and layer-type hybrid CPPs was obtained *via* EDX spectrum profile scanning and elemental mapping data. The EDX spectrum profile scanning data for **Hybrid CPP I** (Figure 2a,b) revealed a typical tendency for a core–shell structure (Fe-MIL-88B@Ga-MIL-88B), as evidenced by the dominance of iron atoms at the center of a particle as a core component (Fe-MIL-88B) and the abundance of gallium atoms at the edge of a particle as a shell constituent (Ga-MIL-88B). Finally, as clearly shown in the elemental mapping data (Figure 2c), iron atoms were only detected at the central part of the particle, while gallium atoms were found in high concentrations at the external regions of the particle. Note that carbon and oxygen atoms were also distributed over the entire particle. The compositional data clearly confirmed the formation of a well-defined core–shell nanostructure in

which the initial rod-shaped Fe-MIL-88B nanoparticles are surrounded by newly grown gallium-based CP (Ga-MIL-88B). This leads us to conclude that the initial Fe-MIL-88B nanoparticles act as a seed for the growth of secondary CP (Ga-MIL-88B). The EDX spectrum profile scanning data obtained for **Hybrid CPP II** (Figure 2d,e) clearly indicated the formation of a layer structure (C/A/C), as evidenced by the detection of iron atoms only at the middle of a particle and the detection of indium atoms only at both tips of a particle. There was no significant concentration of indium atoms detected at the particle center of **Hybrid CPP II** (Figure 2d,e). This result can be compared to the finding of a sufficient concentration of gallium atoms at the center of the core–shell product of **Hybrid CPP I** (Figure 2a,b). Finally, the elemental mapping data (Figure 2f) confirmed again the formation of a C/A/C layer-type nanostructure. The obtained compositional data illustrated that the anisotropic growth of secondary CP (In-MIL-88B) at both tips of the initial Fe-MIL-88B nanoparticles results in the formation of layer-type heterometalated nanoparticles. The N_2 adsorption isotherms of pure Fe-MIL-88B particle, **Hybrid CPP I**, and **Hybrid CPP II** exhibited the behavior for multilayer adsorption. In addition, there was no significant difference in the N_2 adsorption properties of the resulting hybrid CPPs compared to pure Fe-MIL-88B CPP. It is well-known that the MIL-88B family with the extraordinary high flexibility does not show any substantial surface area from N_2 adsorption.³² Therefore, a significant change in the N_2 adsorption properties as a consequence of the alternation of metal ions within MIL-88B structure cannot be expected.

The fact that the newly grown gallium- and indium-based CPs have the hexagonal 3D structure of Ga-MIL-88B and In-MIL-88B consisting of trimers of MO_6 octahedra ($M = \text{Ga or In}$) connected to BDC building blocks (as is the case for the Fe-MIL-88B seed) was verified by powder X-ray diffraction (PXRD) data. The PXRD patterns acquired for **Hybrid CPP I** (Figure 3b) and **II** (Figure 3c) were essentially identical to that of pure Fe-MIL-88B (Figure 3a). On the other hand, the dissimilar growth behavior on the surface of the Fe-MIL-88B seeds, such as the isotropic growth seen with Ga-MIL-88B and the anisotropic growth seen with In-MIL-88B, can be explained by the size variation of the metal ions. The ionic size of Ga(III) is 76.0 pm, which is quite similar to that of Fe(III) at 78.5 pm.³³ However, the ionic size of In(III) is 94.0 pm, which is significantly larger than that of Fe(III).³³ The size difference between the metal ions participating within the MIL-88B structures will give rise to variation in the cell parameters of the MIL-88B structures. First, Ga-MIL-88B may have cell parameters that are quite similar to those of Fe-MIL-88B due to the size similarity between Ga(III) and Fe(III). In fact, the similarity in the cell parameters of Fe-MIL-88B and Ga-MIL-88B was verified by PXRD (Figure 3) and selected area electron diffraction (SAED, Figure 4)

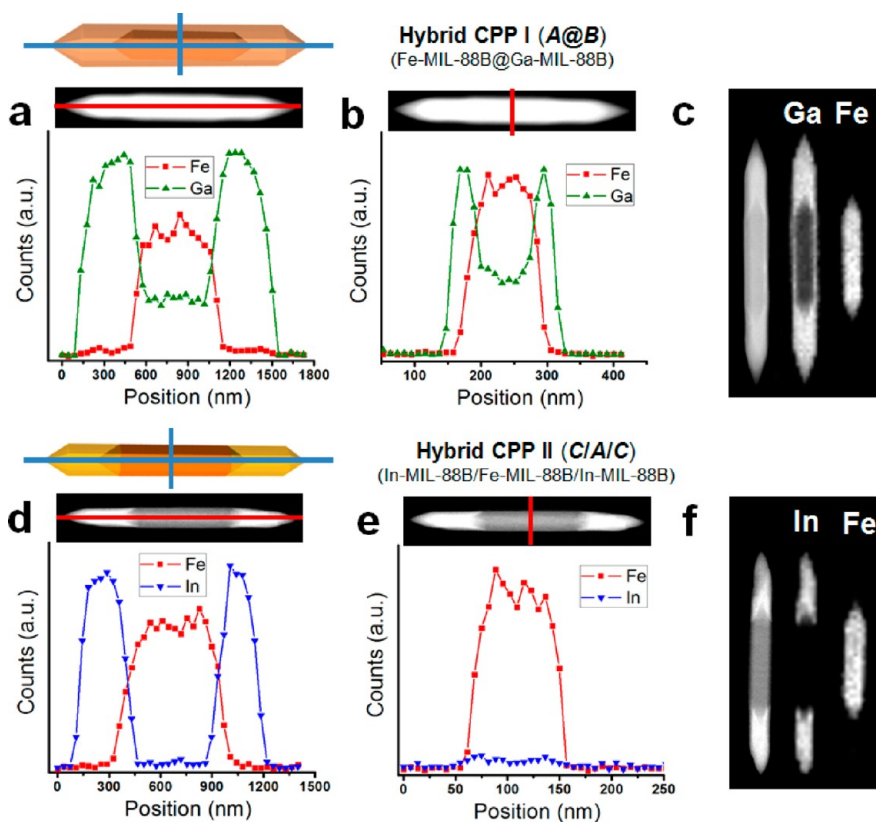


Figure 2. (a,b) EDX spectrum profile scanning and (c) elemental mapping data for core-shell-type Hybrid CPP I. (d,e) EDX spectrum profile scanning and (f) elemental mapping data for layer-type Hybrid CPP II.

data. The good similarity between the cell parameters of the two MIL-88B structures makes it possible to grow Ga-MIL-88B in an isotropic manner on all surfaces of the Fe-MIL-88B seeds. However, In-MIL-88B will have cell parameters that are notably different from those of Fe-MIL-88B, as would be expected considering the size difference between the two metal ions. Such a mismatch will prevent the isotropic growth of In-MIL-88B on Fe-MIL-88B. Indeed, the dissimilar cell parameters of In-MIL-88B were identified by PXRD (Figure 3) and SAED (Figure 4) data.

As shown in Figure 3a,b, the diffraction peaks of **Hybrid CPP I**, which contains both Fe-MIL-88B and Ga-MIL-88B within a single particle, are nearly identical to those of pure Fe-MIL-88B. Such a result indicates that Ga-MIL-88B and Fe-MIL-88B have similar a and c cell parameters ($a = b$ due to the hexagonal structure). The peaks at $2\theta = 9.22^\circ$ and 9.47° (see red box in Figure 3a) in the PXRD pattern of the Fe-MIL-88B nanorods were assigned to the (002) and (100) planes, respectively. Analysis of these peaks yielded c and a cell parameter values of 19.16 and 10.77 Å, respectively. The corresponding peaks at $2\theta = 9.31^\circ$ and 9.57° (see red box in Figure 3b) in the PXRD pattern of **Hybrid CPP I** (Fe-MIL-88B@Ga-MIL-88B) were assigned to the (002) and (100) planes for both Fe-MIL-88B and Ga-MIL-88B. However, two diffraction peaks at $2\theta = 8.95^\circ$ and 9.23° (see red box in Figure 3c) for **Hybrid CPP II** originated from two

(002) planes of In-MIL-88B and Fe-MIL-88B, respectively. The significantly different c cell parameters obtained from these peaks are 19.74 Å for In-MIL-88B and 19.14 Å for Fe-MIL-88B. Just to compare, there is only one peak assigned to the (100) planes at $2\theta = 9.53^\circ$ for both Fe-MIL-88B and In-MIL-88B in the PXRD pattern of **Hybrid CPP II**. These results indicate that the In-MIL-88B within **Hybrid CPP II** has a similar a cell parameter, but a significantly larger c cell parameter when compared to the Fe-MIL-88B seed. In addition, the only peak corresponding to the (004) planes of Ga-MIL-88B and Fe-MIL-88B in the PXRD pattern of **Hybrid CPP I** was observed at $2\theta = 18.58^\circ$ (see blue box in Figure 3b). However, two clear peaks corresponding to the (004) planes of In-MIL-88B and Fe-MIL-88B were observed in the PXRD patterns of **Hybrid CPP II** at $2\theta = 17.82^\circ$ and 18.52° (see blue box in Figure 3c), respectively.

The cell parameters of M-MIL-88B ($M = \text{Fe, Ga, In}$) were also identified by SAED patterns (Figure 4). As revealed in the SAED patterns of **CPP-15** (Figure 4a) and **Hybrid CPP I** (Figure 4b), both Fe-MIL-88B (0.96 nm) and Ga-MIL-88B (0.96 nm) have quite similar d_{002} values, which is consistent with the PXRD data. However, the two SAED patterns obtained at the center and tip of **Hybrid CPP II** revealed that the center region (Fe-MIL-88B part, Figure 4c) and the tip region (In-MIL-88B part, Figure 4d) have different d -spacings.

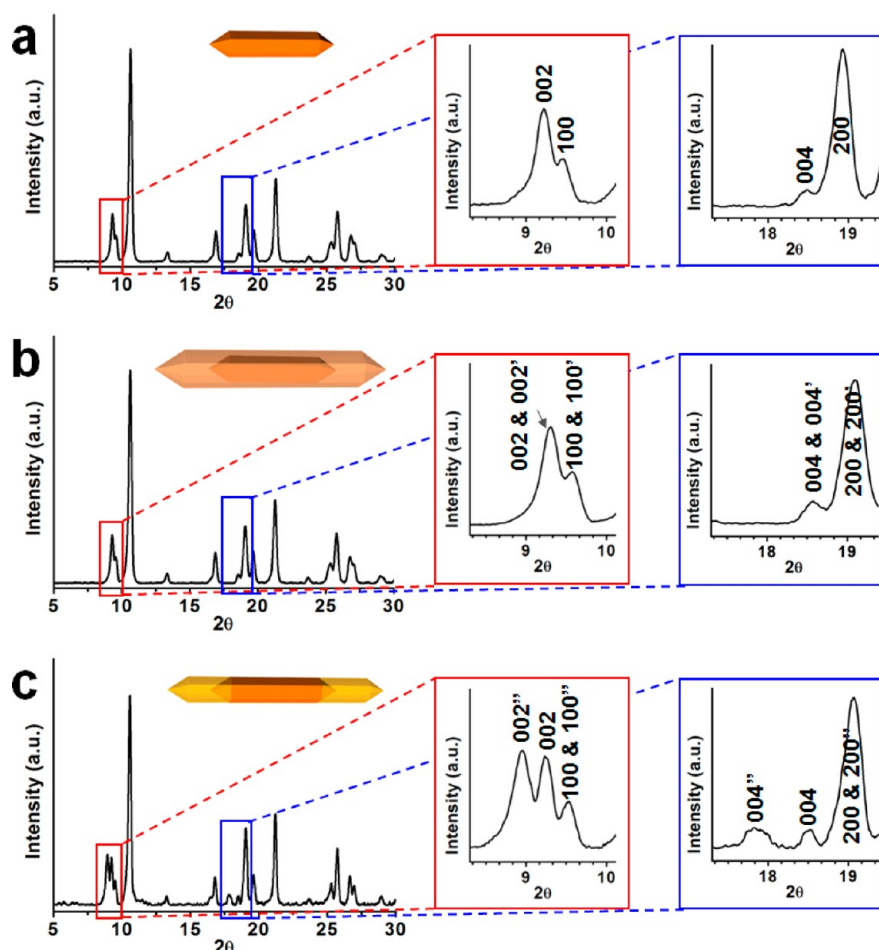


Figure 3. PXRD patterns of (a) CPP-15 (pure Fe-MIL-88B), (b) Hybrid CPP I (hybrid of Fe-MIL-88B and Ga-MIL-88B), and (c) Hybrid CPP II (hybrid of Fe-MIL-88B and In-MIL-88B). Magnified patterns for the selected areas are shown in the insets. Symbols: (') Ga-MIL-88B, (') In-MIL-88B.

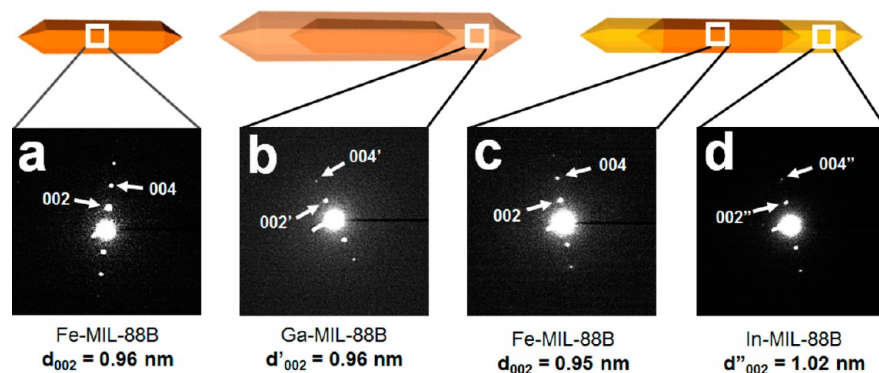


Figure 4. SAED patterns of (a) Fe-MIL-88B obtained from CPP-15 ($d_{002} = 0.96$ nm), (b) Ga-MIL-88B obtained from a tip of Hybrid CPP I ($d'_{002} = 0.96$ nm), (c) Fe-MIL-88B obtained from a center of Hybrid CPP II ($d_{002} = 0.95$ nm), and (d) In-MIL-88B obtained from a tip of Hybrid CPP II ($d''_{002} = 1.02$ nm). Symbols: (') Ga-MIL-88B, (') In-MIL-88B.

In-MIL-88B showed a d''_{002} value of 1.02 nm, which was larger than the d_{002} value of Fe-MIL-88B. This result is in good agreement with the PXRD data, as a larger d''_{002} value indicates a larger c cell parameter value.

As a result of the larger size of In(III) compared to Fe(III), the dimension of a trimer of the InO_6 octahedra within In-MIL-88B will be larger than that in Fe-MIL-88B,

as illustrated in Figure 5a. Consequently, the large size of the InO_6 octahedra can lead to an increase in the a and c cell parameters of In-MIL-88B. Finally, the sizable mismatch in the cell parameters between the original crystal (Fe-MIL-88B) and the secondary crystal (In-MIL-88B) may prevent systematic growth. However, once the initial seed crystal guides the growth of new crystal,

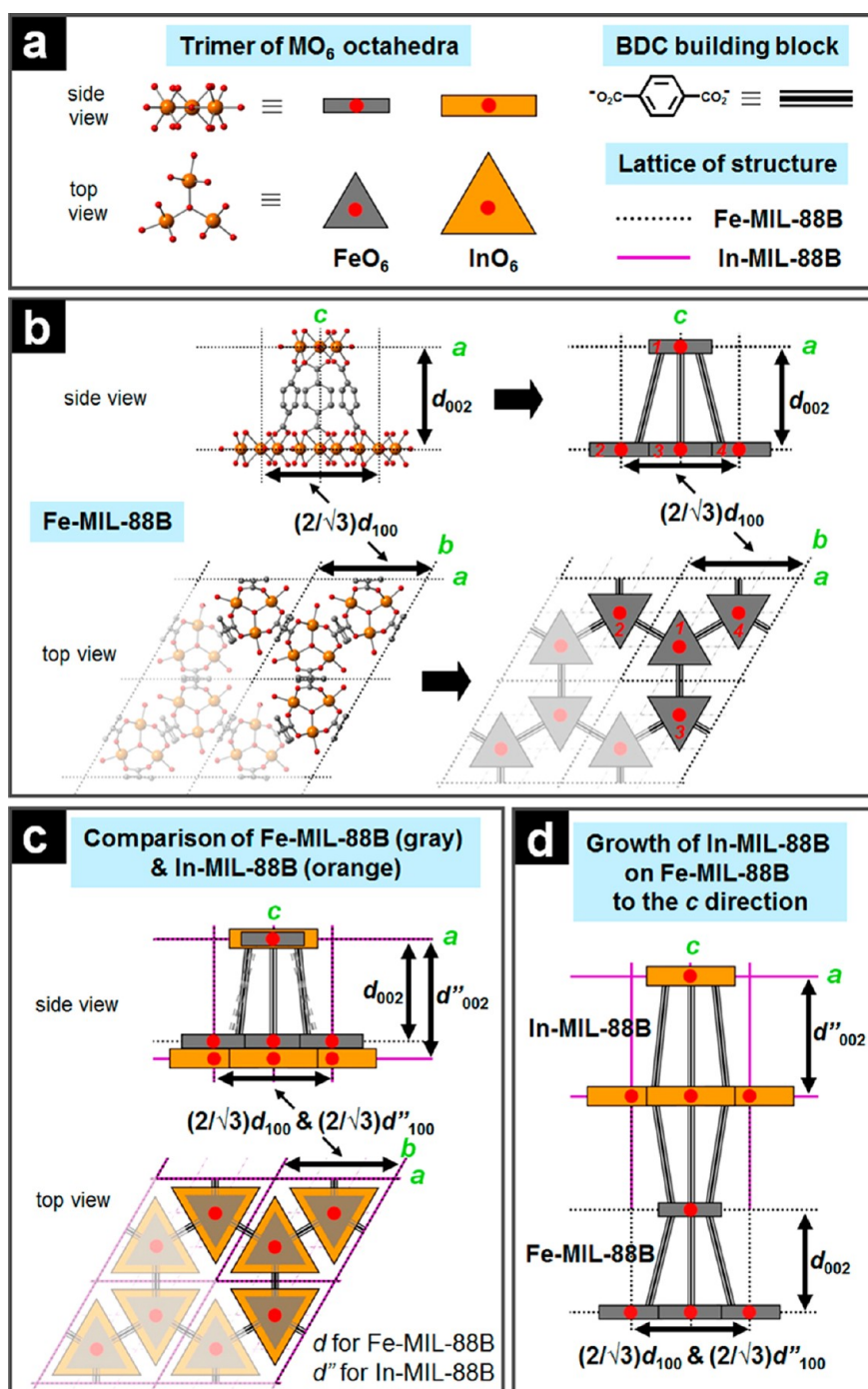


Figure 5. (a) Ball-and-stick and/or schematic representations of trimers of FeO_6 (gray) and InO_6 (orange) octahedras, BDC building block, and lattice of structures. (b) Ball-and-stick (left) and the corresponding simplified schematic representation (right) of the Fe-MIL-88B hexagonal structure. (c) Schematic comparison of the In-MIL-88B structure, which has an enlarged c cell parameter while maintaining the a cell parameter, and the Fe-MIL-88B structure ($d''_{002} > d_{002}$ and $d_{100} = d_{100}$). (d) Schematic representation of the growth of In-MIL-88B on Fe-MIL-88B in the c -direction. Note that two MIL-88B structures have different c cell parameters, but the same a cell parameter.

this mismatch can be rearranged as follow: if only the c cell parameter significantly changes while the a and b cell parameters are somewhat maintained (this was indeed verified by PXRD and SAED, as shown in Figure 3 and 4), which can be induced by the guidance of the initial Fe-MIL-88B crystal structure, then the anisotropic growth of In-MIL-88B will only occur in the c -direction

(Figure 5c,d). In fact, a control experiment revealed that In-MIL-88B was not formed in the absence of Fe-MIL-88B nanorods, which act as seeds and direct the growth of In-MIL-88B. Otherwise, only **CPP-3**,³⁴ which has a Kagomé net structure consisting of $\text{InO}_4(\text{OH})_2$ octahedra known as In-MIL-68,³⁵ was produced. Note that a slight amount of **CPP-3** was formed as a byproduct during the

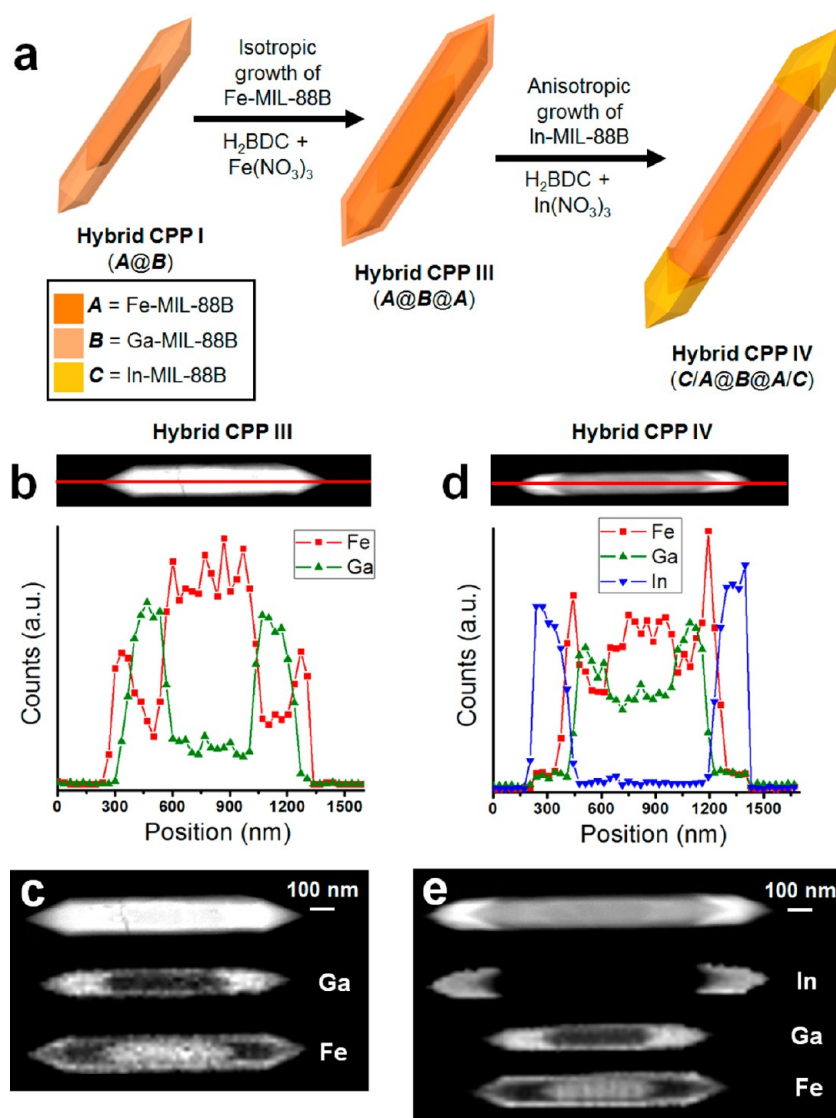


Figure 6. (a) Schematic representation of the preparation of two complicated heterocompositional CPPs, Hybrid CPP III (A@B@A) and Hybrid CPP IV (C/A@B@A/C), through the continuous isotropic and/or anisotropic nanoscale growth of CPs. (b) EDX spectrum profile scanning and (c) elemental mapping data for multi core-shell-type Hybrid CPP III. (d) EDX spectrum profile scanning and (e) elemental mapping data for multicompositional Hybrid CPP IV.

preparation of **Hybrid CPP II**. From this result, we can infer that Fe-MIL-88B induced the formation of In-MIL-88B rather than In-MIL-68. The anisotropic growth of secondary CP in only the *c*-direction at both tips of the seed resulted in the layer-type heterostructure of **Hybrid CPP II**. This seed-directed nanoscale growth approach for the production of hybrid CPPs may be applicable to many coordination polymer systems through the understanding on their cell parameters and structural flexibility. The isotropic nanoscale growth of the secondary CP onto the entire surface of the seed particles can be possible when the cell parameters of the seed CP and the secondary CP are quite similar. On the other hand, a significant difference between the cell parameters of the seed CP and the secondary CP will basically prevent the isotropic growth of the secondary CP on the seed CP; however, the flexibility of the CP structure can allow

the adjustment of some cell parameters of the secondary CP through the guidance of the seed CP structure. This can finally induce the anisotropic growth of the secondary CP onto the seed particles only in the particular direction.

Not only were A@B and C/A/C-type heterocompositional CPPs synthesized *via* a one-time nanoscale growth process, but more sophisticated heterostructures were also fabricated through a series of systematic growth processes. A second procedure for the isotropic growth of Fe-MIL-88B on the surface of **Hybrid CPP I** was performed to induce the formation of multi core-shell type **Hybrid CPP III** (Fe-MIL-88B@Ga-MIL-88B@Fe-MIL-88B, A@B@A, Figure 6a and see Supporting Information Figure S3). This was achieved by conducting an additional solvothermal reaction in the presence of both **Hybrid CPP I** and new precursors (H₂BDC and Fe(NO₃)₃)

for CP growth. The EDX spectrum profile scanning data (Figure 6b) clearly revealed the formation of a multi core–shell structure ($A@B@A$ type), as shown by the dominance of iron atoms at both the center and edge of a particle and the abundance of gallium atoms in the middle of a particle. Furthermore, the elemental mapping data of **Hybrid CPP III** visibly confirmed the formation of an $A@B@A$ type heterostructure (Figure 6c), in which the initial rod-shaped Fe-MIL-88B is located at the center of the particle and is surrounded by the first grown Ga-MIL-88B existing at the exact area between the iron-dominated center and edge. The second grown Fe-MIL-88B is positioned at the very outside of the particle. These compositional data lead us to conclude that **Hybrid CPP I** acts as a seed for the isotropic growth of Fe-MIL-88B. Further anisotropic growth of In-MIL-88B on the surface of **Hybrid CPP III** resulted in a complicated heterostructure (**Hybrid CPP IV**) containing Fe-MIL-88B, Ga-MIL-88B, and In-MIL-88B in the form of $C/A@B@A/C$ (Figure 6a and see Supporting Information Figure S4). One can easily see that the In-MIL-88B was newly grown only at both tips and not on the lateral facets

of **Hybrid CPP III**, as evidenced by the EDX spectrum profile scanning (Figure 6d) and elemental mapping data (Figure 6e).

CONCLUSIONS

The successful fabrication of sophisticated hetero-compositional hybrid CPPs was demonstrated through the precise and controlled isotropic and/or anisotropic nanoscale growth of CPs (M-MIL-88B series, M = Fe, Ga, In). Fe-MIL-88B seeds directed the formation of analogous MIL-88B structures of Ga and In, which could not be easily formed in the absence of Fe-MIL-88B seed. The dissimilar growth behavior, that is, growth in an isotropic or anisotropic fashion, was found to be caused by the size variation among the metal ions within the initial and new CPs. In addition to simple hybrid CPPs, very complicated hybrid CPPs were synthesized *via* the continuous systematic growth of various CPs. The fabrication of well-defined heterostructures is very important for multifunctional materials research and for the fine-tuning of material properties. The results shown here will allow multicompositional nanomaterials to be constructed through the integration of various CPs.

METHODS

Solvents and all other chemicals were obtained from commercial sources and used as-received unless otherwise noted. All scanning electron microscopy (SEM) images were obtained with a JEOL JSM-6701F field-emission SEM. All scanning transmission electron microscopy (STEM) images were acquired on an FEI Tecnai G2 F30 ST using dark-field imaging in STEM mode at 300 kV. Energy dispersive X-ray (EDX) spectra, EDX spectrum profile scanning data, and elemental mapping images were obtained using an STEM attachment (Korea Basic Science Institute in Seoul). All transmission electron microscopy (TEM) images and selected area electron diffraction (SAED) patterns were acquired with a JEOL JEM-2100F at 200 kV (Center for Microcrystal Assembly, Sogang University). X-ray diffraction patterns were obtained using a Rigaku Ultima IV equipped with a graphite-monochromated Cu K α radiation source (40 kV, 40 mA). All PXRD and SAED data for all samples were measured after the same pretreatment (a dynamic vacuum at room temperature for 40 min).

Preparation of CPP-15 (A, Fe-MIL-88B). A precursor solution of 1,4-benzenedicarboxylic acid (3.0 mg, 0.018 mmol) and $\text{Fe}(\text{NO}_3)_3 \cdot 9\text{H}_2\text{O}$ (6.4 mg, 0.016 mmol) in 0.4 mL of *N,N*-dimethylformamide (DMF) was added to 0.4 mL of CH_3CN . The resulting mixture was placed in an oil bath (120 °C) for 40 min. The resulting **CPP-15 (A)** was isolated and subsequently washed with DMF and methanol *via* centrifugation–redispersion cycles. Each successive supernatant was decanted and replaced with fresh methanol.

Preparation of Hybrid CPP I (A@B, Fe-MIL-88B@Ga-MIL-88B). A precursor solution was prepared by mixing 1,4-benzenedicarboxylic acid (3.0 mg, 0.018 mmol) and $\text{Ga}(\text{NO}_3)_3 \cdot x\text{H}_2\text{O}$ (5.1 mg, 0.020 mmol) in 2.0 mL of DMF. The synthesized **CPP-15 (A)** (2.0 mg) was then introduced to the precursor solution. The resulting mixture was placed in an oil bath (100 °C) for 20 min. **Hybrid CPP I (A@B)** generated at this time was isolated and subsequently washed with DMF and methanol *via* centrifugation–redispersion cycles. During the last step, the desired **Hybrid CPP I** was easily separated from the small amount of byproduct.

Preparation of Hybrid CPP II (C/A/C, In-MIL-88B/Fe-MIL-88B/In-MIL-88B). A precursor solution was prepared by mixing 1,4-benzenedicarboxylic acid (3.0 mg, 0.018 mmol) and $\text{In}(\text{NO}_3)_3 \cdot x\text{H}_2\text{O}$ (7.8 mg, 0.020 mmol) in 2.0 mL of DMF. The synthesized **CPP-15 (A)** (2.0 mg) was then introduced to the precursor solution. The

resulting mixture was placed in an oil bath (100 °C) for 20 min. **Hybrid CPP II (C/A/C)** generated at this time was isolated and subsequently washed with DMF and methanol *via* centrifugation–redispersion cycles. During the last step, the desired **Hybrid CPP II** was easily separated from the byproduct of In-MIL-88B.

Preparation of Hybrid CPP III (A@B@A, Fe-MIL-88B@Ga-MIL-88B@Fe-MIL-88B). A precursor solution was prepared by mixing 1,4-benzenedicarboxylic acid (3.0 mg, 0.018 mmol) and $\text{Fe}(\text{NO}_3)_3 \cdot 9\text{H}_2\text{O}$ (6.4 mg, 0.016 mmol) in 0.4 mL of DMF, and added to 0.4 mL of CH_3CN . The synthesized **Hybrid CPP I (A@B)** (2.0 mg) was then introduced to the precursor solution. The resulting mixture was placed in an oil bath (120 °C) for 40 min. **Hybrid CPP III (A@B@A)** generated at this time was isolated and subsequently washed with DMF and methanol *via* centrifugation–redispersion cycles.

Preparation of Hybrid CPP IV (C/A@B@A/C, In-MIL-88B/Fe-MIL-88B@Ga-MIL-88B@Fe-MIL-88B/In-MIL-88B). A precursor solution was prepared by mixing 1,4-benzenedicarboxylic acid (3.0 mg, 0.018 mmol) and $\text{In}(\text{NO}_3)_3 \cdot x\text{H}_2\text{O}$ (7.8 mg, 0.020 mmol) in 2.0 mL of DMF. The synthesized **Hybrid CPP III (A@B@A)** (2.0 mg) was then introduced to the precursor solution. The resulting mixture was placed in an oil bath (100 °C) for 20 min. **Hybrid CPP IV (C/A@B@A/C)** generated at this time was isolated and subsequently washed with DMF and methanol *via* centrifugation–redispersion cycles.

Conflict of Interest: The authors declare no competing financial interest.

Supporting Information Available: SEM, TEM, and STEM images of long **Hybrid CPP II** (Figure S1). A series of EDX spectra obtained from **Hybrid CPP I** and **II** (Figure S2). SEM and TEM images of **Hybrid CPP III** and **IV** (Figure S3 and S4). This material is available free of charge *via* the Internet at <http://pubs.acs.org>.

Acknowledgment. This work was supported by the NLRL Program (no. 2011-0028321) and the WCU program (no. R32-2011-000-10217-0) through NRF grant funded by the MEST.

REFERENCES AND NOTES

1. Furukawa, H.; Ko, N.; Go, Y. B.; Aratani, N.; Choi, S. B.; Choi, E.; Yazaydin, A. Ö.; Snurr, R. Q.; O’Keeffe, M.; Kim, J.; *et al.* Ultrahigh Porosity in Metal–Organic Frameworks. *Science* **2010**, 329, 424–428.

2. Maji, T. K.; Matsuda, R.; Kitagawa, S. A Flexible Interpenetrating Coordination Framework with a Bimodal Porous Functionality. *Nat. Mater.* **2007**, *6*, 142–148.
3. Bloch, E. D.; Queen, W. L.; Krishna, R.; Zadrozny, J. M.; Brown, C. M.; Long, C. R. Hydrocarbon Separations in a Metal–Organic Framework with Open Iron(II) Coordination Sites. *Science* **2012**, *335*, 1606–1610.
4. An, J.; Rosi, N. L. Tuning MOF CO₂ Adsorption Properties via Cation Exchange. *J. Am. Chem. Soc.* **2010**, *132*, 5578–5579.
5. Britt, D.; Furukawa, H.; Wang, B.; Glover, T. G.; Yaghi, O. M. Highly Efficient Separation of Carbon Dioxide by a Metal–Organic Framework Replete with Open Metal Sites. *Proc. Natl. Acad. Sci. U.S.A.* **2009**, *106*, 20637–20640.
6. Song, F.; Wang, C.; Falkowski, J. M.; Ma, L.; Lin, W. Isorecticular Chiral Metal–Organic Frameworks for Asymmetric Alkene Epoxidation: Tuning Catalytic Activity by Controlling Framework Catenation and Varying Open Channel Sizes. *J. Am. Chem. Soc.* **2010**, *132*, 15390–15398.
7. Chen, B.; Xiang, S.; Qian, G. Metal–Organic Frameworks with Functional Pores for Recognition of Small Molecules. *Acc. Chem. Res.* **2010**, *43*, 1115–1124.
8. Oh, M.; Mirkin, C. A. Chemically Tailorable Colloidal Particles from Infinite Coordination Polymers. *Nature* **2005**, *438*, 651–654.
9. Jung, S.; Cho, W.; Lee, H. J.; Oh, M. Self-Template-Directed Formation of Coordination-Polymer Hexagonal Tubes and Rings, and Their Calcination to ZnO Rings. *Angew. Chem., Int. Ed.* **2009**, *48*, 1459–1462.
10. Spokoyny, A. M.; Kim, D.; Sumrein, A.; Mirkin, C. A. Infinite Coordination Polymer Nano- and Microparticle Structures. *Chem. Soc. Rev.* **2009**, *38*, 1218–1227.
11. Ni, Z.; Masel, R. I. Rapid Production of Metal–Organic Frameworks via Microwave-Assisted Solvothermal Synthesis. *J. Am. Chem. Soc.* **2006**, *128*, 12394–12395.
12. Horcajada, P.; Chalati, T.; Serre, C.; Gillet, B.; Sebrie, C.; Baati, T.; Eubank, J. F.; Heurtaux, D.; Clayette, P.; Kreuz, C.; *et al.* Porous Metal–Organic Framework Nanoscale Carriers as a Potential Platform for Drug Delivery and Imaging. *Nat. Mater.* **2010**, *9*, 172–178.
13. Taylor, K. M. L.; Rieter, W. J.; Lin, W. Manganese-Based Nanoscale Metal–Organic Frameworks for Magnetic Resonance Imaging. *J. Am. Chem. Soc.* **2008**, *130*, 14358–14359.
14. Mckinlay, A. C.; Morris, R. E.; Horcajada, P.; Férey, G.; Gref, R.; Couvreur, P.; Serre, C. BioMOFs: Metal–Organic Frameworks for Biological and Medical Applications. *Angew. Chem., Int. Ed.* **2010**, *49*, 6260–6266.
15. Lin, W.; Rieter, W. J.; Taylor, K. M. L. Modular Synthesis of Functional Nanoscale Coordination Polymers. *Angew. Chem., Int. Ed.* **2009**, *48*, 650–658.
16. Carné, A.; Carbonell, C.; Imaz, I.; Maspoch, D. Nanoscale Metal–Organic Materials. *Chem. Soc. Rev.* **2011**, *40*, 291–305.
17. Makiura, R.; Motoyama, S.; Umemura, Y.; Yamanaka, H.; Sakata, O.; Kitagawa, H. Surface Nano-Architecture of a Metal–Organic Framework. *Nat. Mater.* **2010**, *9*, 565–571.
18. Li, Y.-S.; Liang, F.-Y.; Bux, H.; Feldhoff, A.; Yang, W.-S.; Caro, J. Molecular Sieve Membrane: Supported Metal–Organic Framework with High Hydrogen Selectivity. *Angew. Chem., Int. Ed.* **2010**, *49*, 548–551.
19. Liu, B.; Ma, M.; Zacher, D.; Bétard, A.; Yusenko, K.; Metzler-Nolte, N.; Wöll, C.; Fischer, R. A. Chemistry of SURMOFs: Layer-Selective Installation of Functional Groups and Post-Synthetic Covalent Modification Probed by Fluorescence Microscopy. *J. Am. Chem. Soc.* **2011**, *133*, 1734–1737.
20. Lu, G.; Hupp, J. T. Metal–Organic Frameworks as Sensors: A ZIF-8 Based Fabry-Pérot Device as a Selective Sensor for Chemical Vapors and Gases. *J. Am. Chem. Soc.* **2010**, *132*, 7832–7833.
21. Bétard, A.; Fischer, R. A. Metal–Organic Framework Thin Films: From Fundamentals to Applications. *Chem. Rev.* **2012**, *112*, 1055–1083.
22. Furukawa, S.; Hirai, K.; Nakagawa, K.; Takashima, Y.; Matsuda, R.; Tsuruoka, T.; Kondo, M.; Haruki, R.; Tanaka, D.; Sakamoto, H.; *et al.* Heterogeneously Hybridized Porous Coordination Polymer Crystals: Fabrication of Heterometallic Core–Shell Single Crystals with an In-Plane Rotational Epitaxial Relationship. *Angew. Chem., Int. Ed.* **2009**, *48*, 1766–1770.
23. Koh, K.; Wong-Foy, A. G.; Matzger, A. J. MOF@MOF: Microporous Core–Shell Architectures. *Chem. Commun.* **2009**, 6162–6164.
24. Furukawa, S.; Hirai, K.; Takashima, Y.; Nakagawa, K.; Kondo, M.; Tsuruoka, T.; Sakata, O.; Kitagawa, S. A Block PCP Crystal: Anisotropic Hybridization of Porous Coordination Polymers by Face-Selective Epitaxial Growth. *Chem. Commun.* **2009**, 5097–5099.
25. Hirai, K.; Furukawa, S.; Kondo, M.; Uehara, H.; Sakata, O.; Kitagawa, S. Sequential Functionalization of Porous Coordination Polymer Crystals. *Angew. Chem., Int. Ed.* **2011**, *50*, 8057–8061.
26. Costi, R.; Saunders, A. E.; Banin, U. Colloidal Hybrid Nanostructures: A New Type of Functional Materials. *Angew. Chem., Int. Ed.* **2010**, *49*, 4878–4897.
27. Robinson, R. D.; Sadtler, B.; Demchenko, D. O.; Erdonmez, C. K.; Wang, L.-W.; Alivisatos, A. P. Spontaneous Superlattice Formation in Nanorods through Partial Cation Exchange. *Science* **2007**, *317*, 355–358.
28. Habas, S. E.; Lee, H.; Radmilovic, V.; Somorjai, G. A.; Yang, P. Shaping Binary Metal Nanocrystals through Epitaxial Seeded Growth. *Nat. Mater.* **2007**, *6*, 692–697.
29. Zeng, H.; Li, J.; Liu, J. P.; Wang, Z. L.; Sun, S. Exchange-Coupled Nanocomposite Magnets by Nanoparticle Self-Assembly. *Nature* **2002**, *420*, 395–398.
30. Serre, C.; Mellot-Draznieks, C.; Surblé, S.; Audebrand, N.; Filinchuk, Y.; Férey, G. Role of Solvent-Host Interactions that Lead to Very Large Swelling of Hybrid Frameworks. *Science* **2007**, *315*, 1828–1831.
31. Cho, W.; Park, S.; Oh, M. Coordination Polymer Nanorods of Fe-MIL-88B and Their Utilization for Selective Preparation of Hematite and Magnetite Nanorods. *Chem. Commun.* **2011**, *47*, 4138–4140.
32. Horcajada, P.; Salles, F.; Wuttke, S.; Devic, T.; Heurtaux, D.; Maurin, G.; Vimont, A.; Daturi, M.; David, O.; Magnier, E.; *et al.* How Linker's Modification Controls Swelling Properties of Highly Flexible Iron(III) Dicarboxylates MIL-88. *J. Am. Chem. Soc.* **2011**, *133*, 17839–17847.
33. Shannon, R. D. Revised Effective Ionic Radii and Systematic Studies of Interatomic Distances in Halides and Chalcogenides. *Acta Crystallogr.* **1976**, *A32*, 751–767.
34. Cho, W.; Lee, H. J.; Oh, M. Growth-Controlled Formation of Porous Coordination Polymer Particles. *J. Am. Chem. Soc.* **2008**, *130*, 16943–16946.
35. Volklinger, C.; Meddouri, M.; Loiseau, T.; Guillou, N.; Marrot, J.; Férey, G.; Haouas, M.; Taulelle, F.; Audebrand, N.; Latroche, M. The Kagomé Topology of the Gallium and Indium Metal–Organic Framework Types with a MIL-68 Structure: Synthesis, XRD, Solid-State NMR Characterizations, and Hydrogen Adsorption. *Inorg. Chem.* **2008**, *47*, 11892–11901.